

Quantum suppression of cold reactions far from the s -wave energy limit

Or Katz,^{1,*} Meirav Pinkas,² Nitzan Akerman,² Ming Li,³ and Roez Ozeri²

¹*School of Applied and Engineering Physics, Cornell University, Ithaca, NY 14853.*

²*Department of Physics of Complex Systems, Weizmann Institute of Science, Rehovot 7610001, Israel*

³*Atom Computing, Inc., 2500 55th St, Suite 100, Boulder, Colorado 80301, USA*

(Dated: January 31, 2025)

Reactions between pairs of atoms are ubiquitous processes in chemistry and physics. Quantum scattering effects on reactions often require extremely ultracold temperatures, approaching the s -wave regime, with a small number of partial waves involved. At higher temperatures, the different phases associated with the centrifugal barriers of different partial waves average out quantum interference to yield classical reaction rates. Here, we use quantum-logic to experimentally study resonant charge-exchange reactions between individual cold pairs of neutral ^{87}Rb atoms and optically-inaccessible $^{87}\text{Rb}^+$ ions far above the s -wave regime. We find that the measured charge-exchange rate is significantly suppressed with respect to the classical prediction. Our results indicate that even at temperatures three orders of magnitude higher than the ultracold s -wave regime, quantum interference in collisions persists and impacts reaction rates.

I. INTRODUCTION

Studies of chemical reactions between pairs of atoms are of great practical and fundamental importance in the chemical and physical sciences. At ultracold temperatures, the wave-like nature of the reactants strongly influences the rates and pathways of reactions. Quantum-mechanical effects such as shape resonances [1] or Feshbach resonances [2, 3] can enhance or suppress reaction rates, provide control over the interaction strength, and allow for precise experimental calibration of the molecular potentials that are otherwise hard to compute. Beyond their fundamental importance, quantum scattering resonances play a role in enabling control over interactions in quantum simulators [4–6] and are used to push the limits of precision quantum sensors [7, 8].

Quantum scattering effects between pairs of atoms are, however, mostly limited to identical particles [9, 10] or to ultracold temperatures, where only a few partial waves are involved [11–17]. Partial waves refer to the quantized angular momentum components of the colliding pair, characterized by the quantum number l . The matter-wave length scale for entering the s -wave scattering regime ($l = 0$) in collisions of neutral atoms is typically a few nanometers, which for typical atomic masses translates to an energy scale of hundreds of $k_B \times \mu\text{K}$. At short internuclear distances where significant overlap between the colliding bodies often occurs, the energies of the van der Waals interaction and centrifugal interaction become comparable. Consequently, the scattering phases acquired during collisions on different partial waves are largely distinct. The interference of multiple partial waves on thermally averaged reaction rate coefficients tends to average out, yielding a classical result.

Collisions between a neutral atom and a charged ion, on the other hand, are governed by the long-range polarization potential. This potential imposes a matter-wave length scale of hundreds of nanometers to enter the s -wave regime, corresponding to sub- μK temperatures for most atom-ion pairs [15, 16, 18–21]. At these internuclear distances, where the contribution of centrifugal interactions is significant and the overlap of atomic wavefunctions remains minimal, inelastic or reactive processes are suppressed unless a shape or Feshbach resonance condition is satisfied. By contrast, at short-range molecular distances, where the overlap of atomic wavefunctions becomes substantial, such processes predominantly occur, and the partial-wave dependence becomes less significant. It has thus been predicted that resonant inelastic and reactive processes, such as the exchange of electronic spins or the exchange of charge between identical nuclei [22, 23], could feature quantum signatures that persist at much higher temperatures. This mechanism, known as the partial-wave phase-locking mechanism, originates from the fact that the scattering phase differences between many partial waves and the s -wave are nearly identical, leading to s -wave behavior and quantum interference phenomena far outside the s -wave regime.

Hybrid atom-ion platforms provide great experimental control, with the ability to resolve single collision events between pairs of atoms [18, 24–45]. These features make them excellent candidates for studying the phase-locking mechanism and identifying signatures of s -wave scattering in cross sections measured at much higher energies. Such platforms also enable the exploration of properties that are otherwise difficult to compute using *ab initio* approaches. In recent years, we have studied the cross sections of inelastic processes between $^{88}\text{Sr}^+$ ions and other Sr^+ isotopes, which lie far from the s -wave regime and could exhibit the phase-locking mechanism [23, 29, 45–47]. However, accurately

* Corresponding author: or.katz@cornell.edu

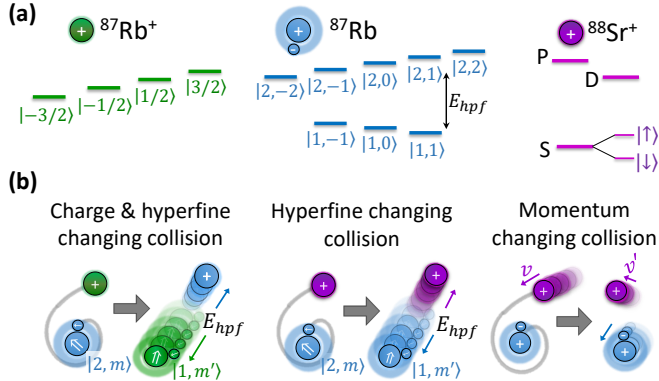


Figure 1. Atom-ion cold collisional processes and spin structure. (a) Nuclear spin structure of $^{87}\text{Rb}^+$ (left), hyperfine structure of ^{87}Rb in its electronic ground-state (middle) and ground and first excited state manifolds for spin-1/2 $^{88}\text{Sr}^+$ (right). Before a collision, the $^{88}\text{Sr}^+$ ion is initialized in its ground-state. Both ions lack hyperfine structure because the nuclear (electron) spin of $^{88}\text{Sr}^+$ ($^{87}\text{Rb}^+$) is zero. (b) Resonant charge-exchange reactions between ^{87}Rb – $^{87}\text{Rb}^+$ (left) and spin-exchange collisions between ^{87}Rb – $^{88}\text{Sr}^+$ (middle) can both change the hyperfine state of the neutral atom and convert the internal hyperfine energy E_{hpf} into kinetic motion of the bodies. For an applied magnetic field of 3 G, the change in motion due to transitions between magnetic levels is negligible compared to heating caused by hyperfine de-excitation of the neutral ^{87}Rb atom.

Elastic collisions of an ion with a neutral atom (right) conserve the total momentum of the pair but change the trapped ion’s momentum.

estimating cross sections, which is essential for extracting parameters for theoretical models or comparing with classical values, has been challenging due to uncertainties in the atom-ion experimental collision rate. These uncertainties stem, for example, from the number density of the neutral atom cloud. In Ref. [48], we characterized a systematic mechanism that substantially enhances the collision rate through trap-induced dynamics at low temperatures. This mechanism renders number-density estimations in the absence of ions insufficient for determining the atom-ion collision rate across a wide range of trap parameters. The lack of a reliable technique for estimating the experimental collision rate in the presence of the trap has hindered past experiments from conclusively identifying the phase-locking mechanism in atom-ion pairs.

Here we study experimentally and theoretically resonant charge-exchange reactions between ultracold ^{87}Rb atoms and a cold $^{87}\text{Rb}^+$ ion. Although $^{87}\text{Rb}^+$ lacks optical transitions for direct cooling or detection, we measure its reaction using a quantum-logic technique that employs an auxiliary $^{88}\text{Sr}^+$ logic ion [47]. We develop and demonstrate a method to determine the Langevin-collision probability experienced by the ion through measurements of momentum-changing collisions. This

approach enables estimation of the reaction probability in terms of the Langevin collision rate. We theoretically analyze the scattering using Multi-channel Quantum Defect Theory (MQDT), incorporating the *ab initio* calculated partial-wave dependence. Remarkably, our experimental results align with these theoretical predictions, yet they are incompatible with the classical reaction rate, which is 12 times higher. Notably, this work represents the first experimental observation of the phase-locking mechanism between collisions of a single neutral atom and its parent ion, providing a unique insight into the properties of the quantum *s*-wave regime at temperatures that are more than three orders of magnitude away. The techniques demonstrated here can be readily extended to study other processes, species, and systems.

II. ATOM-ION COLLISIONS

Collision dynamics and outcomes between pairs of atoms strongly depend on their interaction potential. The interaction between a neutral atom and a singly-ionized ion at an internuclear distance R is composed of two terms which dominate at different length scales. At long distances, the electric field of the ion’s charge induces an electric dipole moment of the neutral atom and results in an attractive polarization potential that scales as $-1/R^4$, and depends only on the neutral atom polarizability [18]. This polarization potential becomes the dominant inter-atomic interaction as $R \rightarrow \infty$. If the initial angular momentum is not too large, in a classical framework, this attractive potential leads to an inward spiraling of the pair, known as Langevin collision, until a close contact is made [19, 49, 50].

At short internuclear distances, non-universal chemical forces, dominate the interaction due to significant wavefunction overlap. These forces can lead to inelastic or reactive processes, such as spin exchange, charge exchange, or even molecular association of the colliding particles [18]. In cold atom-ion systems, scattering events that involve a considerable change in the external or internal properties of the complex are typically correlated with Langevin collision events. As a result, the rate of such processes is generally proportional to the Langevin rate [51–53].

In this work, we focus on charge-exchange collisions, reactions in which the nuclei of the ion and neutral atom are exchanged. For heteronuclear species, the charge exchange rate is attenuated by the difference in binding energy of the electron to the two nuclei [54–57]. For homonuclear species, however, the energy mismatch vanishes, making the process resonant and potentially efficient [54, 58–60].

In the case of a neutral alkali-metal atom in the ground state colliding with its parent ion, the atom

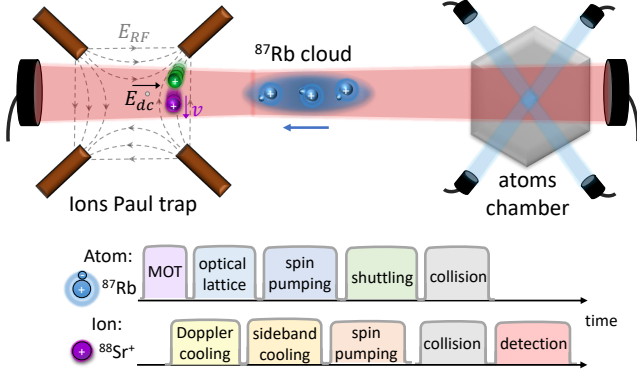


Figure 2. **Experimental Apparatus and Protocol.** We trap neutral ^{87}Rb atoms in the right chamber and short crystals of $^{87}\text{Rb}^+$ and $^{88}\text{Sr}^+$ ions in the left chamber. The ion crystal is laser-cooled near the motional ground-state. We load an atomic cloud into an off-resonant optical lattice dipole trap and shuttle it through the ion’s Paul trap to allow for a collision. For experiments measuring hyperfine changing collisions excess micromotion is compensated. In contrast, for experiments measuring momentum-changing collisions, a time-independent electric field, E_{dc} , displaces the ions from the RF null of the trap, imparting excess micromotion energy along the RF field lines.

is in the $^2S_{1/2}$ state while the ion is in the 1S_0 state when they are sufficiently apart. The atom-ion system is described by two electronic Born-Oppenheimer (BO) states, the *gerade*, g , and the *ungerade*, u , states. These states, which exhibit even and odd symmetries under inversion of electronic coordinates, are denoted by the molecular term symbols $^2\Sigma_{g,u}^+$ respectively. The resonant charge-exchange process then arises from the difference in the scattering phase shifts between the *gerade* and *ungerade* components of the wave-function of the colliding nuclei. The resonant charge-exchange cross section, in the absence of hyperfine interaction, is given by [51, 61, 62]

$$\sigma_{\text{ex}} = \frac{\pi}{k^2} \sum_{l=0}^{\infty} (2l+1) \sin^2(\delta_g^{(l)} - \delta_u^{(l)}), \quad (1)$$

where $\delta_{g,u}^{(l)}$ are the scattering phase shifts of single-channel wave-functions for the BO potential g or u with partial wave l and k is the wavenumber defined as $k = \sqrt{2\mu E}/\hbar$. Since different partial waves are decoupled, and Eq. (1) depends only on single-channel phase shifts, the prototypical resonant charge-exchange problem is fundamentally single-channel in nature.

Resonant charge-exchange collisions between a neutral atom and its parent ion do not alter the ion’s species but can be detected through changes in its external or internal degrees of freedom. At relatively high collision energies or temperatures, (typically more than tens of Kelvin for $^{87}\text{Rb}^+ - ^{87}\text{Rb}$), such processes can be ef-

ficiently observed through either momentum exchange [63–65] or spin transfer, [66, 67]. However, at lower energies within the cold Langevin regime, identifying resonant charge-exchange processes by their induced momentum change becomes challenging [68] [69], unless the atom and ion are distinct isotopes [24].

We probe charge-exchange collisions between cold $^{87}\text{Rb}^+$ and ^{87}Rb pairs by monitoring changes in the spin state after the collision. The ion $^{87}\text{Rb}^+$ has a nuclear spin of $3/2$ and features four nearly degenerate spin levels, owing to its weak nuclear gyromagnetic ratio [70]. The neutral ^{87}Rb atom, in contrast, possesses an additional electron with spin $1/2$, which is strongly coupled to the nuclear spin through the hyperfine interaction ($E_{\text{hpf}} = 328 k_B \times \text{mK}$). When far apart from the ion, the hyperfine interaction ensures that the total spin of the rubidium atom and its projection along the magnetic field axis are good quantum numbers, denoted by F and M . The level structure of these atoms in the electronic ground state is shown in Fig. 1.

During a homonuclear charge-exchange collision, the nuclear spin of the $^{87}\text{Rb}^+$ ion is abruptly swapped with that of the neutral ^{87}Rb atom, which can result in the projection of the neutral from the upper hyperfine manifold ($F = 2$) into the lower one ($F = 1$). This transition, which we call hyperfine de-excitation resonant charge-exchange (HDRCE) process, is accompanied by the release of the internal hyperfine energy and its conversion into kinetic energy of the colliding bodies, as illustrated in Fig. 1. It essentially remains a resonant charge-exchange problem because it relies on the interference between the two short range molecular *gerade* and *ungerade* channels.

However, since these molecular channels do not diagonalize the hyperfine interaction, especially when the atom and the ion are far apart, the HDRCE problem cannot be directly reduced to an effective single channel problem like the prototypical resonant charge-exchange problem. To better understand the experimental HDRCE results, especially in the cold temperature regime where the collision energies are comparable or smaller than the atomic hyperfine interaction energy, it is necessary to properly incorporate the hyperfine interaction in a multi-channel formalism.

In Sec. III, we present our experimental study of the hyperfine de-excitation charge-exchange rate between $^{87}\text{Rb}^+$ and ^{87}Rb pairs, and in Sec. IV, we detail the theoretical framework to analyze this multichannel problem, providing conceptual and quantitative understanding of the hyperfine de-excitation process. In Sec. V we present the results and in Sec. VI discuss their implications.

III. EXPERIMENTAL STUDY

A. Apparatus

We study the interaction between neutral ^{87}Rb atoms and $^{87}\text{Rb}^+$. Two vacuum chambers positioned 25 cm apart are used to trap and laser-cool a cloud of ^{87}Rb atoms to a few μK (right chamber), and to trap short chains of ions cooled near their ground-state in a Paul trap (left chamber) as shown in Fig. 2. The neutral cloud is initially trapped in a magneto-optical trap and subsequently loaded into an off-resonant optical lattice, where the spin state $|F, M\rangle$ of the ^{87}Rb atoms is determined using optical pumping and microwave pulses.

Owing to the closed electronic shell structure of $^{87}\text{Rb}^+$, it lacks the necessary optical transitions that could enable its direct cooling and detection. Instead, we load and trap in a Paul trap [71] a two-ion crystal that is composed of one $^{88}\text{Sr}^+$ and one $^{87}\text{Rb}^+$ via subsequent photo-ionization of a neutral Sr and neutral ^{87}Rb gas. We use the $^{88}\text{Sr}^+$ ion to laser-cool and sympathetically cool all motional modes of the crystal near the ground-state, to compensate for excess micromotion, to enable logic detection of exothermic processes of $^{87}\text{Rb}^+$, and to calibrate the Langevin collision rate with neutral ^{87}Rb atoms. We routinely verify the masses of the two ions via mass spectrometry. Further details on our experimental apparatus can be found in Refs. [46, 47, 72].

The experiment follows the sequence presented in Fig. 2. A cold neutral cloud, with a temperature of a few μK , is shuttled towards the Paul trap at a speed of 24 cm/s in the lab frame by varying the relative optical frequencies of two counter-propagating optical lattice beams. This enables interaction between an ion and, on average, one atom during each passage of the sparse atomic cloud through the Paul trap. The $^{88}\text{Sr}^+$ is initialized in the spin-up state, while the ^{87}Rb are prepared in each of the $|F, M\rangle$ spin states in the electronic ground state in a randomized manner over time. The spin of the $^{87}\text{Rb}^+$ is assumed to be in a completely mixed state.

B. Logic detection of hyperfine de-excitation

During the passage of the atomic cloud, neutral ^{87}Rb atoms may collide with one of the ions. For atoms initialized in the upper hyperfine manifold ($F = 2$), certain collisions result in hyperfine de-excitation, releasing energy into the motional degrees of freedom and causing heating of the ion crystal. Under an applied magnetic field of $B = 3$ G, the change in magnetic energy is negligible compared to the hyperfine energy, making the energy released via hyperfine de-excitation similar for either ion; see Fig. 1. However, the mechanisms are different: in $^{87}\text{Rb} - ^{87}\text{Rb}^+$ collisions, hyper-

fine de-excitation arises primarily from resonant charge-exchange, where the two colliding nuclei are swapped, altering the spin configuration of the resulting individual particles. In contrast, in $^{87}\text{Rb} - ^{88}\text{Sr}^+$ collisions, hyperfine de-excitation occurs through spin-exchange between the two valence electrons, with no transfer of electrons between the nuclei, with weaker contributions from spin relaxation [23]. For simplicity, we refer to $^{87}\text{Rb} - ^{88}\text{Sr}^+$ processes collectively as spin exchange, though our analysis does not assume or exclude specific relaxation channels.

We measure the probability of these energetic collisions using the quantum-logic technique developed in Ref. [47], employing carrier-shelving thermometry. This technique maps hot (cold) motional states of the crystal to a bright (dark) state of the logic ion, which is then detected via state-dependent fluorescence of the logic ion. We use the same experimental parameters as in Ref. [47], which provide high sensitivity (approximately $\eta = 80\%$ detection efficiency) to hyperfine energy release E_{hpf} , in the range of hundreds of $k_{\text{B}} \times \text{mK}$. In contrast, sensitivity to low-energy processes ($\lesssim 1 k_{\text{B}} \times \text{mK}$), such as trap-induced heating [19, 20] or the release of magnetic energy from spin-changing collisions without hyperfine transitions [48], remains low.

In Fig. 3a, the gray bars show the probability P_b that the logic ion in a $^{88}\text{Sr}^+ - ^{87}\text{Rb}^+$ crystal appears bright after one passage of the ^{87}Rb cloud, indicating that the crystal is hot. To differentiate the contributions of charge exchange and spin exchange, we conduct additional measurements. First, we repeat the experiment using a crystal composed of two spin-up $^{88}\text{Sr}^+$ ions and a ^{87}Rb cloud initialized in a spin state $|F = 2, M\rangle$. The purple bars in Fig. 3a show the probability that at least one of the $^{88}\text{Sr}^+$ ions appears bright after a single cloud passage. Second, for both ion crystal configurations, we estimate the readout error probability of our detection technique, which is associated with processes not involving hyperfine de-excitation of ^{87}Rb atoms. To estimate these small errors, we repeat the experiments while preparing the neutral ^{87}Rb atoms in $|1, 1\rangle$ or $|1, -1\rangle$ spin states, where hyperfine-changing collisions are strongly suppressed by energy conservation. The measured probabilities for these control states, shown in Fig. 3a, are less than 2% per $^{88}\text{Sr}^+$ ion on average for both configurations.

Using these measurements, we calculate the hyperfine de-excitation probabilities $\bar{P}_{\text{hpf}}^{(\text{Sr})}$ (for spin exchange) and $\bar{P}_{\text{hpf}}^{(\text{Rb})}$ (for charge exchange) for a single $^{88}\text{Sr}^+$ or $^{87}\text{Rb}^+$ ion interacting with a neutral ^{87}Rb atom in the upper hyperfine state $F = 2$. For each configuration, we define the average error probability as $\epsilon = \frac{1}{2}(P_b(1, 1) + P_b(1, -1))$ where $P_b(F, M)$ denotes the measured probability of a bright event when the neutral ^{87}Rb atom is initialized in $|F, M\rangle$. The probability

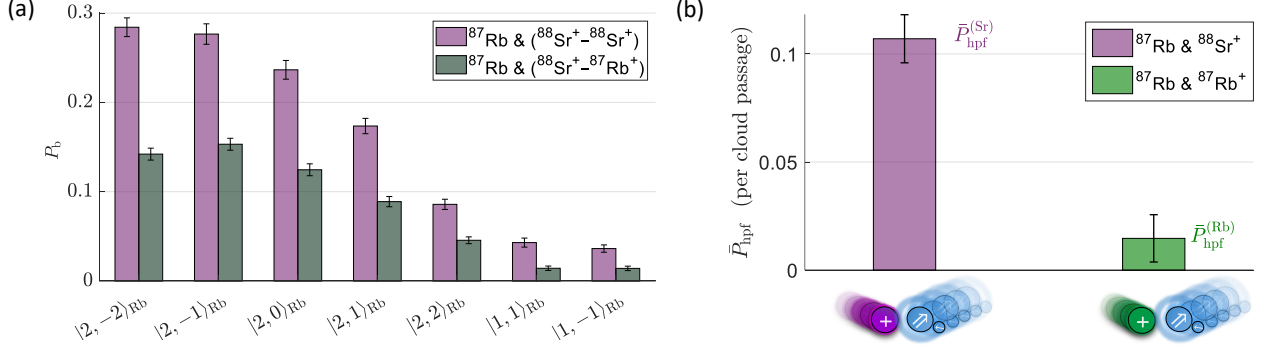


Figure 3. **Hyperfine de-excitation probability and logic detection.** (a) Raw measured probabilities of heating in a two-ion crystal are shown for two configurations: a $^{87}\text{Rb}^+ - ^{88}\text{Sr}^+$ crystal (gray) and a $^{88}\text{Sr}^+ - ^{88}\text{Sr}^+$ crystal (purple). These measurements are taken after passage of a cloud of neutral ^{87}Rb atoms initialized in the $|F, M\rangle$ spin state. The probabilities are measured using a quantum logic detection scheme, where a bright state of a $^{88}\text{Sr}^+$ logic ion indicates a hot event: primarily hyperfine-changing collisions for $F = 2$ or errors associated with other processes for $F = 1$ (see text). (b) Processed probabilities distinguishing between hyperfine de-excitation of ^{87}Rb due to spin exchange with a $^{88}\text{Sr}^+$ ion (purple) or charge exchange with a $^{87}\text{Rb}^+$ ion (green). The quantum logic technique separates these contributions from the data in (a); see text for details. Probabilities in (b) are given per ion per passage of the atomic cloud through the ion trap and are averaged over the spin states of the neutral ^{87}Rb atom in the $F = 2$ manifold. Bars represent 1σ binomial uncertainties.

$\bar{P}_{\text{hpf}}^{(\text{Sr})}$ is determined from the data collected using the $^{88}\text{Sr}^+ - ^{88}\text{Sr}^+$ crystal and is calculated as

$$\bar{P}_{\text{hpf}}^{(\text{Sr})} = \frac{1}{\eta \tilde{M} N_{\text{Sr}}} \sum_{M=-2}^2 (P_b(2, M) - \epsilon), \quad (2)$$

where P_b and ϵ correspond to the purple bars in Fig. 3a. This calculation subtracts the average error ϵ and averages probabilities over the $\tilde{M} = 5$ spin states in the upper hyperfine manifold. It then normalizes by the detection efficiency η and divides by the number of logic ions $N_{\text{Sr}} = 2$.

To estimate the probability $\bar{P}_{\text{hpf}}^{(\text{Rb})}$, we subtract the spin-exchange contribution from the $^{88}\text{Sr}^+ - ^{87}\text{Rb}^+$ crystal measurements:

$$\bar{P}_{\text{hpf}}^{(\text{Rb})} = \frac{1}{5\eta} \left(\sum_{M=-2}^2 (P_b(2, M) - \epsilon) \right) - \bar{P}_{\text{hpf}}^{(\text{Sr})}, \quad (3)$$

where P_b and ϵ refer to the gray bars in Fig. 3a. In Fig. 3b, we present the probabilities $\bar{P}_{\text{hpf}}^{(\text{Sr})}$ and $\bar{P}_{\text{hpf}}^{(\text{Rb})}$. Evidently, the hyperfine-changing collision probability between a single pair of $^{87}\text{Rb}^+ - ^{87}\text{Rb}$ (green bar) is almost an order of magnitude smaller than the hyperfine-changing probability between a single pair of $^{88}\text{Sr}^+ - ^{87}\text{Rb}$ (purple bar).

C. Estimation of the rate coefficient

The previous measurements provided the probabilities for charge-exchange collisions in our system but not the rate coefficient. The relation between the reaction

probability and its rate coefficient depends on specific experimental parameters, such as the local neutral atom density [16, 18, 23, 24, 33], the size and speed of the cloud [46], and ion trap parameters that may contribute to the formation of quasi-bound states [48, 73]. In this subsection, we introduce and detail a technique for estimating the rate of momentum-changing collisions *in situ*, based on atom-ion dynamics with excess micromotion. This method enables us to convert the measured hyperfine de-excitation probability, $\bar{P}_{\text{hpf}}^{(\text{Rb})}$, into a rate coefficient. Such a conversion is essential for direct comparison with theoretical predictions that describe the phase-locking mechanism.

Our calibration relies on the measurement of the momentum-changing collision rate [74, 75], which corresponds to elastic scattering events with large scattering angles [76] as schematically shown in Fig. 1b. These collisions lead to the redistribution of the kinetic energy of the colliding bodies in an approximately isotropic manner, and are usually considered in the context of buffer-gas cooling [74, 77] or ion mobility [60]. Momentum-changing collisions are correlated with Langevin collisions, and their rate coefficient is similar to the Langevin collision rate coefficient [74, 77]. Therefore, the measurement of momentum-changing collisions allows for direct estimation of the Langevin probability and provides an accurate rate estimation.

The technique applies a constant electric field, \vec{E}_{dc} , displacing an ion from the RF-null line by \vec{x} and increasing its excess micromotion energy, E_{EMM} . For our Paul trap, these quantities are given by

$$x_i = \frac{eE_{\text{DC},i}}{m_{\text{ion}}\omega_i^2}, \quad (4)$$

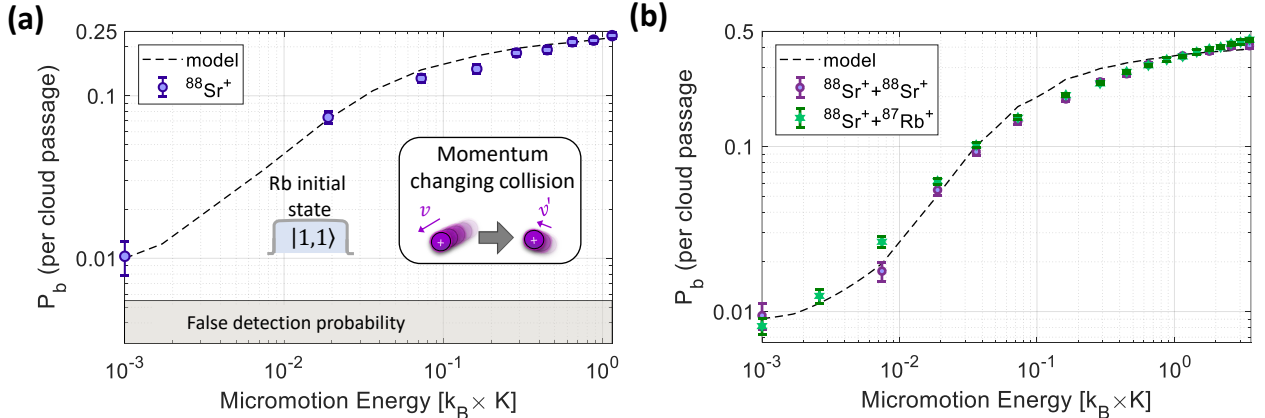


Figure 4. **Momentum changing collisions.** These collisions convert the micromotion energy of an ion into secular motion, detectable with a probability P_b per passage of the cloud. (a) Single ion crystal of $^{88}\text{Sr}^+$. (b) Two-ion crystals of $^{88}\text{Sr}^+ - ^{88}\text{Sr}^+$ (purple) and $^{88}\text{Sr}^+ - ^{87}\text{Rb}^+$ (green). Dashed lines correspond to numerically simulated values, indicating an average Langevin collision rate per ion of $\kappa_L = 0.29 \pm 0.02$ per cloud passage. Bars represent 1σ binomial uncertainties.

and

$$E_{\text{EMM}} = \frac{1}{16} \sum_i m_{\text{ion}} \Omega^2 q_i^2 x_i^2. \quad (5)$$

Here, ω_i denotes the secular trap frequency along each axis ($i \in \{x, y, z\}$), Ω is the RF drive frequency, e is the electron charge, and m_{ion} is the ion's mass. The coefficients q_i denote the trap parameters from the Mathieu equation, which describe the ion's inherent micromotion [78]. For our segmented blade trap, the parameters are $0.45 \text{ MHz} \leq \omega_i \leq 1.5 \text{ MHz}$, $\Omega = 26.5 \text{ MHz}$, $q_y = -q_x \approx 0.14$ with negligible q_z .

We experimentally control x_i by adjusting the voltage V on one of the trap electrodes to generate an electric field along $(\hat{x} + \hat{y})\sqrt{2}$, as illustrated schematically in Fig. 2. The linear dependence of $x_i(V)$ is calibrated by imaging the ion position at various voltages, enabling the precise estimation of the excess micromotion energy, E_{EMM} , through Eq. (5). Importantly, cooling and shelving processes remain highly efficient even at large micromotion amplitudes. This is achieved by aligning the shelving (674 nm) and cooling (422 nm) laser beams perpendicular to the micromotion axis and ensuring that $\omega_i \ll \Omega$.

A momentum-changing collision with a neutral atom redistributes the ion's micromotion energy into secular motion, leading to ion heating [50]. To study this effect, we repeat the previous experiments, shuttling the neutral atom cloud through the ion trap while varying the excess micromotion energy. The neutral atoms are prepared in their lowest-energy spin state, $|1, 1\rangle$, to suppress other heating channels, such as hyperfine de-excitation. After the cloud passes through the trap, we apply carrier-shelving thermometry, mapping the crystal's motional energy to its internal states. Hot ion crystals (with increased secular motion) correspond to

bright ion states, which are measured with a probability P_b per passage of the neutral atom cloud.

In Fig. 4a we present the measured heating probability P_b for a single $^{88}\text{Sr}^+$ ion as a function of the excess micromotion energy, E_{EMM} . The gray-shaded area represents the background probability (0.5%), measured in the absence of the atomic cloud. We extend the experiment to two additional configurations: a $^{88}\text{Sr}^+ - ^{88}\text{Sr}^+$ crystal (purple) and a $^{88}\text{Sr}^+ - ^{87}\text{Rb}^+$ crystal (green), as shown in Fig. 4b. Clearly, higher micromotion energy correlates with an increased rate of momentum-changing collisions.

We use these data to estimate the collision rate by calibrating a model that numerically simulates collision dynamics in our trap under excess micromotion, extending previous numerical models [20, 47, 48]. This model, detailed in Appendix A, has only two free parameters: the ion's effective temperature, T , at the onset of a collision, and the average number of collisions per ion, κ_L , per passage of the cloud through the trap. The effective temperature predominantly determines the probability P_b at low E_{EMM} values, while κ_L primarily influences P_b at higher E_{EMM} values. We find good agreement between the data and the theoretical model for $T = 0.6 \pm 0.1 \text{ mK}$ and $\kappa_L = 0.29 \pm 0.02$, corresponding to the black dashed curves in Fig. 4. The estimated collision temperature exceeds the energy associated with the shuttling speed of the cloud (approximately $E = 0.15 k_B \times \text{mK}$ in the atom-ion center-of-mass frame), which we attribute primarily to trap-induced heating [19, 20]. Additionally, from Fig. 4b, we estimate the ratio $\kappa_L^{\text{Rb}^+} / \kappa_L^{\text{Sr}^+} = 0.97 \pm 0.06$, which is in excellent agreement with the theoretical prediction of approximately 1.

Using the calibrated model, and the measured value of $\bar{P}_{\text{hpf}}^{(\text{Rb})}$ in Fig. 3b, we directly estimate the probabil-

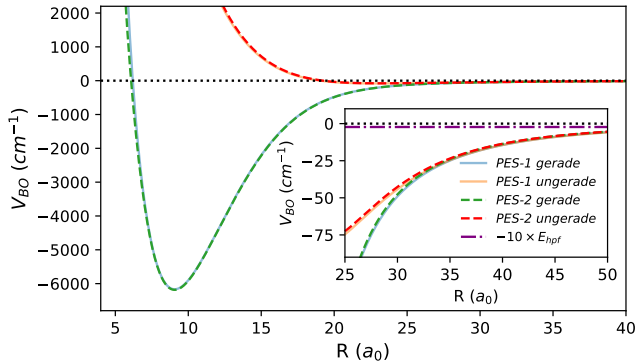


Figure 5. **Born-Oppenheimer potential energy surfaces.** Two publicly available potential energy surfaces for the $^{87}\text{Rb} - ^{87}\text{Rb}^+$ complex are shown in the short-range region. The solid lines represent PES-1, constructed using the data provided with Ref. [79]. The dashed lines represent PES-2, constructed using the data and program provided in Ref. [80]. The inset shows a magnified comparison of the BO potentials and the atomic hyperfine energy of ^{87}Rb , scaled by a factor of 10, in the range of internuclear separation where the electronic wavefunction overlap between the two colliding particles diminishes exponentially.

ity of hyperfine de-excitation via charge-exchange collisions relative to the probability of a Langevin collision in free space; see Appendix A for details. This analysis takes into account trap-induced dynamics, including the formation of quasi-bound states [48, 73]. We find that the hyperfine de-excitation rate coefficient is $k_{\text{de-ex}} = (0.015 \pm 0.012)k_{\text{Langevin}}$ for $^{87}\text{Rb}^+$ and ^{87}Rb , where $k_{\text{Langevin}} = 2.446 \times 10^{-9} \text{ cm}^3/\text{s}$ denotes the Langevin rate coefficient for these atoms in free space. This result is shown in Fig. 6a by the solid black point.

IV. THEORETICAL FRAMEWORK

We theoretically study the hyperfine de-excitation resonant charge-exchange (HDRCE) process between $^{87}\text{Rb} - ^{87}\text{Rb}^+$ using multichannel quantum defect theory (MQDT). In particular, we follow the methodology outlined in Refs. [81, 82] to analyze the suppression of the hyperfine de-excitation process and provide a quantitative framework for understanding the phase-locking mechanism.

This section is organized as follows: in Subsection IV A, we describe the dependence of HDRCE on scattering properties. Subsection IV B presents the MQDT framework for modeling the scattering. In Subsection IV C, we identify the main free parameters in the model relevant to HDRCE and discuss which parameters can be accurately estimated from *ab-initio* calculations and which require experimental measurement. Subsection IV D focuses on thermal averaging and dis-

cusses various approximations for cross sections, including the classical estimate we compare to in the next Section.

A. Hyperfine de-excitation resonant charge-exchange process

We consider the HDRCE process in free space between a fermionic-nucleus neutral atom in a $^2S_{1/2}$ state and its ion in a 1S_0 state. This is a good approximation when the external magnetic field is low such that the Zeeman splittings in the ground states are much smaller than the atomic hyperfine splitting. We explicitly account for the adiabatic electronic interaction under the BO approximation and the hyperfine interaction to describe the colliding particles. The Hamiltonian is isotropic and different partial waves l are decoupled from each other. The total angular momentum of the system $\vec{F} = \vec{l} + \vec{F}_{\text{tot}}$, is conserved where \vec{F}_{tot} is the total “spin” angular momentum. Thus l and F_{tot} are both good quantum numbers.

There are two asymptotic energetically distinct channels in the low magnetic field limit, referred to as “fragmentation channels”, whose eigenstates at large internuclear separations R correspond to the neutral atom in either of the hyperfine states $F = I \pm 1/2$ and the ion in $F_{\text{ion}} = I$. These channels are energetically separated by the atomic ground hyperfine splitting E_{hpf} , in the limit $R \rightarrow \infty$. The HDRCE process arises from the coupling between these channels as the atom and ion approach each other.

For the higher-energy initial atomic hyperfine state ($F = I + 1/2$), the total HDRCE cross section is given by [81, 82]

$$\sigma_{\text{de-ex}}(E) = \frac{\pi \sum_{F_{\text{tot}}} l(2l+1)(2F_{\text{tot}}+1) |S_{01}^{F_{\text{tot}}l}(E)|^2}{(2I+2)(2I+1)k_i^2}, \quad (6)$$

where $S_{01}^{F_{\text{tot}}l}(E)$ is the off-diagonal matrix element of the two-by-two scattering matrix S , defined for angular momentum F_{tot} and partial wave l at energy E . Here we use index 0(1) to represent the energetically lower (higher) fragmentation channel. k_i is the wavenumber with respect to the initial channel, i.e., $k_i = \sqrt{2\mu E_i}/\hbar$ and $E_i = E - E_{\text{hpf}}$ is the initial kinetic energy with respect to channel 1.

At large internuclear separation R , the BO interaction is dominated by long-range dispersion interactions, notably the polarization interaction, which is independent of the atom’s hyperfine state [60]. Consequently, the two fragmentation channels experience the same BO potential and do not couple at long range. However, at shorter R , the two fragmentation channels begin to couple due to the non-zero overlap of the electronic wave-

functions of the colliding bodies. In this regime, it is often more convenient to represent quantities in the molecular basis channels, where the adiabatic molecular electronic potentials are represented by a diagonal matrix, with matrix elements given by linear combinations of the BO potentials [81–83]. The unitary transformation between the fragmentation channels and the molecular basis channels is given by [81, 82]

$$U^{F_{\text{tot}}} = \frac{(-1)^{2F_{\text{tot}}+1}}{\sqrt{2(2I+1)}} \quad (7)$$

$$\times \begin{pmatrix} -\sqrt{2I - F_{\text{tot}} + 1/2} & \sqrt{2I + F_{\text{tot}} + 3/2} \\ \sqrt{2I + F_{\text{tot}} + 3/2} & \sqrt{2I - F_{\text{tot}} + 1/2} \end{pmatrix}.$$

Figure 5 presents two sets of publicly available BO potential energies for the $^{87}\text{Rb} - ^{87}\text{Rb}^+$ complex, derived from *ab initio* electronic structure calculations [79, 80]. On the scale shown, the two sets of potentials appear nearly identical. The inset highlights the comparison between the BO potentials and E_{hpf} in the range of R where the electronic wavefunctions overlap diminishes rapidly with increasing R ; this range is characterized by the exponential decay of the difference between the BO potentials, resulting from electronic exchange interaction [60]. In this intermediate region, where the short-range potentials transition to the long-range regime, the hyperfine interaction is already at least an order of magnitude smaller than the electronic potentials.

For each partial wave l , the diagonal matrix elements of the Hamiltonian include a long-range centrifugal barrier term $l(l+1)\hbar^2/2\mu R^2$, and an attractive polarization potential, $-\alpha/2R^4$. Here, μ is the reduced mass, and α is the static polarizability of the atom in the ground $^2S_{1/2}$ state. For rubidium, we use the value from [84], $\alpha = 319.8$ a.u., which is experimentally determined [85].

For a given collision energy E , we define $L(E)$ as the highest partial wave for which the centrifugal barrier height is lower than E . At the estimated experimental temperature of 0.6 mK, L is approximately 12. When the entrance kinetic energy exceeds the centrifugal barrier ($l \leq L$), the short-range region is classically accessible, and the HDRCE process is predominantly semi-classical. Near the peak of the centrifugal barrier, quantum reflection [86] can modify the semi-classical picture. Conversely, for $l > L$, the short-range region becomes classically inaccessible, and hyperfine de-excitation can only occur via quantum tunneling [86]. These two quantum processes, reflection and tunneling, typically manifest as resonance structures in cross sections. As E moves farther from the peak of the barrier for a given partial wave, these resonances become narrower and less significant.

B. MQDT for resonant charge-exchange with hyperfine interaction

Following the principles of the original quantum defect theory (QDT) for Coulomb interactions [87–91], multichannel quantum defect theory (MQDT) provides a framework for describing resonant charge-exchange collisions [81, 82]. It achieves this by capturing the short-range physics through a set of short-range parameters and treating the long-range interaction, dominated by the polarization potential, via exact solutions. When different partial waves are decoupled, as in this work, the scattering matrix S for energetically open channels, at a given energy E and partial wave l , can be expressed in terms of the real and symmetric reaction matrix K :

$$S = (\mathbb{1} + iK)(\mathbb{1} - iK)^{-1}, \quad (8)$$

where $\mathbb{1}$ is the identity matrix.

The reaction matrix K is derived by connecting the short-range part, represented by the short-range reaction matrix K^c , to the long-range analytic solution, given by the matrices Z^c . This relationship is given by the matrix equation [92],

$$K = -(Z_{fc}^c - Z_{gc}^c K^c)(Z_{fs}^c - Z_{gs}^c K^c)^{-1}. \quad (9)$$

Since the inter-atomic interaction considered here is isotropic, and hyperfine de-excitation occurs when both asymptotic channels are open, Eq. (9) reduces to a 2×2 matrix equation for each combination of E and l . Furthermore, because the fragmentation channels are uncoupled at the long range, it is more convenient to represent Eq. (9) in these channels, where the Z^c matrices are diagonal. The diagonal matrix elements correspond to the exact solutions of the single channel Schrödinger equations for the long-range potential, incorporating the associated hyperfine interaction energies:

$$Z_{ab}^c(E, l) = \begin{pmatrix} Z_{ab}^c(E, l) & 0 \\ 0 & Z_{ab}^c(E - E_{\text{hpf}}, l) \end{pmatrix}, \quad (10)$$

where the subscripts $ab \in \{fs, fc, gs, gc\}$. For a purely long-range polarization potential, the Z^c matrix elements are provided in Ref. [93]. For convenience, the four Z^c functions for a specific channel can be compactly represented as a matrix

$$Z^c = \begin{pmatrix} Z_{fs}^c & Z_{fc}^c \\ Z_{gs}^c & Z_{gc}^c \end{pmatrix}. \quad (11)$$

The physics of the short-range interaction is encapsulated in the effective K^c matrix. In principle, this matrix has three independent short-range parameters that are specific to each combination of E and l . However, we simplify the analysis, by introducing two approximations that reduce the number of parameters to a globally defined set of four (with the parameters independent of

E and l). These four short-range parameters, together with known quantities such as the atomic hyperfine interaction energy and static polarizability, can accurately describe the scattering and quantum resonance properties over a broad energy range near the threshold where the magnitude of energy E is small.

The first approximation relies on the observation that the magnitude of the hyperfine interaction is much smaller than the magnitude of the electronic potential energies in the short-range region (see inset in Fig. 5). Therefore, we neglect the hyperfine interaction in the short range, rendering the Hamiltonian diagonal in the molecular basis channels. Consequently, the K^c matrix is also diagonal in the molecular basis channels and is related to the K^c matrix in the fragmentation channels by a unitary transformation [81, 82]

$$K^c = U^{F_{\text{tot}}\dagger} K^{c(\text{mol})} U^{F_{\text{tot}}} , \quad (12)$$

where $K^{c(\text{mol})} = \text{diag}(K_+, K_-)$ denotes the K^c matrix in the molecular basis channels. Its diagonal elements are given by

$$K_{\pm} = \frac{1}{2}(K_g^c + K_u^c \pm (-1)^{F_{\text{tot}}+l-1/2}(K_g^c - K_u^c)). \quad (13)$$

Here, $K_{g,u}^c$ are the single-channel K^c matrix elements associated with the *gerade* and the *ungerade* BO potentials, respectively. These elements are related to the single-channel short-range phase shifts $\delta_{g,u}^s$ and quantum defects $\mu_{g,u}$ by [86]

$$K_{g,u}^c = \tan \delta_{g,u}^s = \tan(\pi\mu_{g,u} + \pi/4). \quad (14)$$

If greater accuracy is required, the hyperfine interaction at short range can be treated perturbatively, modifying $K^{c(\text{mol})}$ to include the effect of such a perturbation.

The second approximation assumes that, in the cold and ultracold collision regime, the short-range phases (or quantum defects) are independent of the collision energy E and linear in $(l+1/2)^2$. This can be expressed as

$$\delta_{g,u}^s(E, l) = \pi \left[\mu_{g,u}^{(0)} + (l+1/2)^2 \beta_{g,u} + 1/4 \right], \quad (15)$$

where $\mu_{g,u}^{(0)}$ are the zero-energy, zero-partial-wave quantum defects, and $\beta_{g,u}$ describe the partial-wave dependence of the short-range phases. The validity of the approximation is supported by two observations. First, the range of collision energies of interest is much smaller than the BO potentials in the short range. Second, the angular momentum term in the Hamiltonian, which scales linearly with $(l+1/2)^2$, is also small enough to be treated as a perturbation [81, 82]. At higher collision energies, outside the regime relevant to our experiment, additional corrections may be necessary; one can introduce perturbative terms linear in E , and $\delta_{g,u}^s$ can be expanded further in higher-order combinations of E and $(l+1/2)^2$.

C. MQDT short-range parameters

The four short-range parameters, $\mu_g^{(0)}, \mu_u^{(0)}, \beta_g$ and β_u , required for calculating scattering properties at low energies via MQDT, can be estimated through a combination of experimental data fitting and numerical modeling based on *ab initio* potential energy curves. In particular, we highlight that only the values of β_g and β_u , which determine the partial wave dependence, can be reliably derived from theoretical considerations. In contrast $\mu_g^{(0)}$ and $\mu_u^{(0)}$ which determine the s -wave scattering lengths, require experimental calibration.

We use a WKB-type semi-classical method to extract the short-range parameters, because the kinetic energy in the short-range region is typically large. The WKB scattering phase for a collision energy E and partial wave l , assuming a single classical turning point at R_{min} is expressed as

$$\delta_{g,u}^{s(\text{WKB})} = \int_{R_{\text{min}}}^{\infty} \sqrt{2\mu(E - V_{g,u}) - \frac{l(l+1)}{R^2}} dR - \int_{0+}^{\infty} \sqrt{2\mu(E - \frac{\alpha}{2R^4}) - \frac{l(l+1)}{R^2}} dR. \quad (16)$$

By calculating $\delta_{g,u}^{s(\text{WKB})}$ for various l and E , the results are fitted to Eq. (15) (or higher-order expansions) to extract the short range parameters. We obtained $\beta_g = 2.9 \times 10^{-4}$ and $\beta_u = 4.7 \times 10^{-4}$ (with $\mu_g^{(0)} = 286.89$ and $\mu_u^{(0)} = 77.38$) for PES-1 [79], and $\beta_g = 2.5 \times 10^{-4}$ and $\beta_u = 4.2 \times 10^{-4}$ (with $\mu_g^{(0)} = 288.12$ and $\mu_u^{(0)} = 75.49$) for PES-1 [79].

The parameters β_g and β_u are perturbative quantities with absolute values much smaller than one. Their estimation from BO potentials is more reliable than that of $\mu_g^{(0)}, \mu_u^{(0)}$, particularly at low partial-wave regimes where $\beta L^2 \lesssim 1$. For the $^{87}\text{Rb} - ^{87}\text{Rb}^+$ complex, the β values, and specifically the uncertainty in $\beta_u - \beta_g$, are sufficiently small such that their contribution to the rate coefficient is limited. As shown in subsequent sections, this manifests as the phase-locking mechanism. For all subsequent calculations, we adopted the β_g and β_u values from PES-2 but confirmed that using the PES-1 values does not alter the conclusions of this work.

The theoretical estimation of the quantum defects $\mu_g^{(0)}, \mu_u^{(0)}$ is unreliable due to several reasons. State-of-the-art quantum chemistry methods and basis sets often lack the precision needed to predict these parameters accurately. Because the function $K_{g,u}^c$ has a periodicity of one with respect to the quantum defects, only the digits after the decimal point significantly influence scattering properties. Moreover, quantum defects or scattering lengths derived directly from BO potentials may fail to account for certain non-BO effects in the short range. For example, as demonstrated in Ref. [94] for

hydrogen-proton collisions, short-range hyperfine interactions and nonadiabatic couplings can modify the scattering lengths derived from BO potentials. Although these effects can still be incorporated into MQDT by adjusting the short-range parameters, they render extractions based solely on adiabatic BO potential surfaces invalid.

Thus, estimating the quantum defects for $^{87}\text{Rb} - ^{87}\text{Rb}^+$ requires experimental input. Traditionally, ultracold scattering properties, such as the s -wave scattering lengths, directly translate to the zero-energy, zero-partial-wave short-range phases. Alternatively, the locations of resonances in elastic cross sections [81] or near-threshold bound-state energies [95] could serve as data for fitting the parameters in the MQDT model. However, for $^{87}\text{Rb} - ^{87}\text{Rb}^+$, obtaining such measurements is experimentally challenging.

Estimating these parameters from thermally averaged scattering properties, which are experimentally more accessible (e.g., rate coefficients), poses additional challenges, particularly outside the ultracold regime. The difficulty arises because thermal averaging involves contributions from many energies and partial waves, which tend to obscure characteristic features like resonances. Nevertheless, the phase-locking mechanism enables us to estimate the difference between $\mu_g^{(0)}$ and $\mu_u^{(0)}$ from our experimental results, as detailed in the next subsections.

In certain calculations describing HDRCE at higher temperatures, the approximation in Eq. (15) requires higher-order terms in energy and partial wave. To extend the validity of these calculations, we extract the energy and partial-wave dependence directly from PES-2 while correcting the low-energy phases using Eq. (16), such that

$$\delta_{g,u}^s(E, l) \approx \delta_{g,u}^{s(\text{WKB})}(E, l) - \delta_{g,u}^{s(\text{WKB})}(0, 0) + \pi\mu_{g,u}^{(0)}. \quad (17)$$

D. Thermally averaged reaction rate coefficient and semi-classical approximation

To compare with experimental results, the thermally-averaged reaction rate coefficient is calculated by integrating the HDRCE cross section with a one-dimensional velocity distribution:

$$k_{\text{de-ex}}(T) = \int_0^\infty e^{-E_i/k_B T} v \sigma_{\text{de-ex}}(E) dv, \quad (18)$$

where k_B is the Boltzmann constant, and $v = \sqrt{2E_i/\mu}$ is the relative velocity between the colliding particles. In practice, the integration is performed up to a velocity corresponding to an energy of at least $10 \times k_B T$.

We now consider a few approximations to simplify the structure of the thermally-averaged rate coefficient and provide physical intuition. First, we apply a

semi-classical approximation to the long-range \mathcal{Z}^c functions [86]

$$\mathcal{Z}^c \approx \begin{pmatrix} \cos \bar{\delta}_l^c & -\sin \bar{\delta}_l^c \\ \sin \bar{\delta}_l^c & \cos \bar{\delta}_l^c \end{pmatrix}, \quad (19)$$

where $\bar{\delta}_l^c$ is the semiclassical phase shift arising from the long-range potential. There are two phases corresponding to the energies in the two fragmentation channels, e.g. see Eq. (10), and they are highly sensitive to energy and partial-wave. Using the framework in Subsections IV A and IV B, and assuming only classically allowed partial waves contribute semi-classically, the HDRCE cross-section can be approximated as:

$$\bar{\sigma}_{\text{de-ex}}(E) = \frac{\pi}{k_i^2} \frac{I}{2I+1} \sum_{l=0}^{L(E)} (2l+1) \sin^2(\delta_g^s - \delta_u^s). \quad (20)$$

Eq. (20) is similar to the results in Ref. [51], but with a key difference: the phase difference in the sine function corresponds to the two short-range phases, rather than the long-range elastic scattering phases of the two fragmentation channels. Since the short-range phases are largely insensitive to energy and partial waves (see Eq. (15)), the semi-classical cross sections manifest the phase-locking characteristics.

There are a few caveats to Eq. (20). First, it does not account for quantum reflection and tunneling, which can generate resonance structures in the cross section. Second, the summation over l goes to $L(E)$, a step function, effectively coarse-graining all energies corresponding to the same $L(E)$ into a single semi-classical cross section. However, both the resonance effects and energy coarse-graining are less pronounced after thermal averaging.

We can further approximate Eq. (20) by neglecting the partial-wave dependence, as originally assumed in Ref. [22]. This yields:

$$\bar{\sigma}_{\text{de-ex}}(E) \approx \frac{I}{2I+1} \sigma_{\text{Langevin}}(E) \sin^2 \left[\pi(\mu_g^{(0)} - \mu_u^{(0)}) \right], \quad (21)$$

where $\sigma_{\text{Langevin}}(E) = 2\pi\sqrt{\alpha/2E_i}$ is the classical Langevin cross section [22], calculated with respect to the entrance channel associated with the higher atomic hyperfine energy ($F = I + 1/2$ manifold of the neutral atom). In this approximation, the magnitude of the cross section depends on the difference between the quantum defects, becoming minimal when $\mu_g^{(0)} = \mu_u^{(0)}$ and maximal when $\mu_g^{(0)} = \mu_u^{(0)} \pm \frac{1}{2}$.

It is also insightful to consider the opposite limit, where many partial waves contribute, and the partial-wave dependence completely scrambles the short-range phases. In this case, the $\sin^2(\delta_g^s - \delta_u^s)$ terms in Eq. (20) can be assumed to average to $1/2$ [53, 60], a simplification known as the Degenerate Internal State Approximation (DISA). Under this assumption, the classical

limit is given by

$$\bar{\sigma}_{\text{de-ex}}(E) \rightarrow \frac{I}{2(2I+1)} \sigma_{\text{Langevin}}(E). \quad (22)$$

Interestingly, Eq. (22) has been established previously in the context of charge-exchange cross sections. In the classical approximation, the resonant charge-exchange cross section satisfies $\sigma_{\text{ex}} \approx \sigma_{\text{Langevin}}/2$ [53, 60], and accounting for spin statistics, the HDRCE cross section between atom-ion pairs with nuclear spin I is given by $\sigma_{\text{de-ex}} \approx \sigma_{\text{ex}}I/(2I+1)$ [51, 82]. We note that this model does not account for the contribution of glancing collisions, which, at temperatures significantly higher than those considered in this work (e.g., at or above 100 K for Rb [65]), could have a substantial impact.

V. RESULTS

Using the theoretical tools from the previous section, we investigate what the experimentally measured HDRCE rate coefficient reveals. Figure 6 presents the experimental measurement overlaid with theoretically calculated rate coefficients based on different approximations and different short-range parameter sets.

In Fig. 6(a), we compare four different theoretical calculations, each evaluated with three sets of $\mu_{g,u}^{(0)}$ represented by the colors blue, orange, and green. The four theoretical models we used are: the full MQDT calculation with partial-wave dependent short-range parameters (solid lines), the full MQDT calculation without partial-wave dependent short-range parameters (dashed lines), the semi-classical approximation using Eq. (20) with partial-wave dependent short-range parameters (dotted lines), and the semi-classical approximation using Eq. (21) that is partial-wave independent (dash-dotted lines). The four models produce quantitatively similar results for each set of $\mu_g^{(0)}$ and $\mu_u^{(0)}$ shown in the figure. They all exhibit the phase-locking characteristic, where the rate coefficients remain approximately constant with increasing temperature, even though more partial waves are involved. Closer inspection shows that the partial-wave dependent short-range parameters play a more significant role at higher temperatures, while the semi-classical approximation deviate more in the lower temperature regime, particularly when the overall rate-coefficient is high.

The classical limit (Eq. 22) is represented by the black dash-dotted line, and the experimentally measured data point is shown as black circle, with error bars along both x- and y-axes. The experimental data point overlaps with the set of short range parameters represented in green, where $\mu_g^{(0)} = -0.30$ and $\mu_u^{(0)} = -0.35$, corresponding to an absolute difference of $|\mu_g^{(0)} - \mu_u^{(0)}| = 0.05$. Since $\mu^{(0)}$ denotes the zero partial wave parameter,

this result provides insight into scattering in the s -wave regime.

To explore the breakdown of the phase-locking mechanism at higher temperatures, we employ the semi-classical approximation to examine the full landscape of the rate coefficient. Using Eq. (17), we compute the dependence of the thermally averaged rate coefficient on the phase difference $\mu_g^{(0)} - \mu_u^{(0)}$ and temperature, as presented in Fig. 6b.

The solid black, dashed gray, and white dotted contours in the figure correspond to the center, upper bound, and lower bound values of the measured rate coefficient. These contours delineate the approximate regions of $\mu_g^{(0)} - \mu_u^{(0)}$ that fit the experimental data. The measured value signifies significant suppression of the HDRCE process and a small difference in $|\mu_g^{(0)} - \mu_u^{(0)}|$. At higher temperatures, (approximately $T \gtrsim 0.05$ K), the range of parameter values consistent with the experimental data vanishes. This aligns with expectations, as increasing collision energy disrupts the phase-locking mechanism due to the change in the short-range phase difference for higher partial waves. With enough partial waves contributing and the energy dependence becoming significant, the short-range phase differences across different l values become sufficiently randomized. Consequently at $T \gtrsim 1$ K we observe the onset of convergence toward the classical limit described in Eq. (22), irrespective of the zero-energy, zero-partial-wave short-range parameters.

VI. DISCUSSION AND OUTLOOK

In this work, we analyzed hyperfine de-excitation in resonant charge-exchange collisions between atom-ion pairs of $^{87}\text{Rb} - ^{87}\text{Rb}^+$ by monitoring the ion temperature using an auxiliary $^{88}\text{Sr}^+$ logic ion. We probed momentum-changing collisions to estimate the Langevin collision rate in our setup and to establish an absolute scale for the resonant charge-exchange rate. Our theoretical analysis demonstrates that hyperfine de-excitation process in resonant charge-exchange collisions is well-described by quantum mechanical scattering and is significantly suppressed compared to both the Langevin rate and the classical hyperfine de-excitation rate.

We attribute the suppression of hyperfine de-excitation to the phase-locking mechanism [22, 23], which suggests a breakdown of the Degenerate Internal State Approximation (DISA). This breakdown leads to coherent contributions of phase scattering across different partial waves, deviating from the incoherent behavior assumed in the classical regime and Eq. (22). Instead, the resonant exchange dynamics align not only with the full MQDT framework, which directly computes the leading partial wave dependence from ab

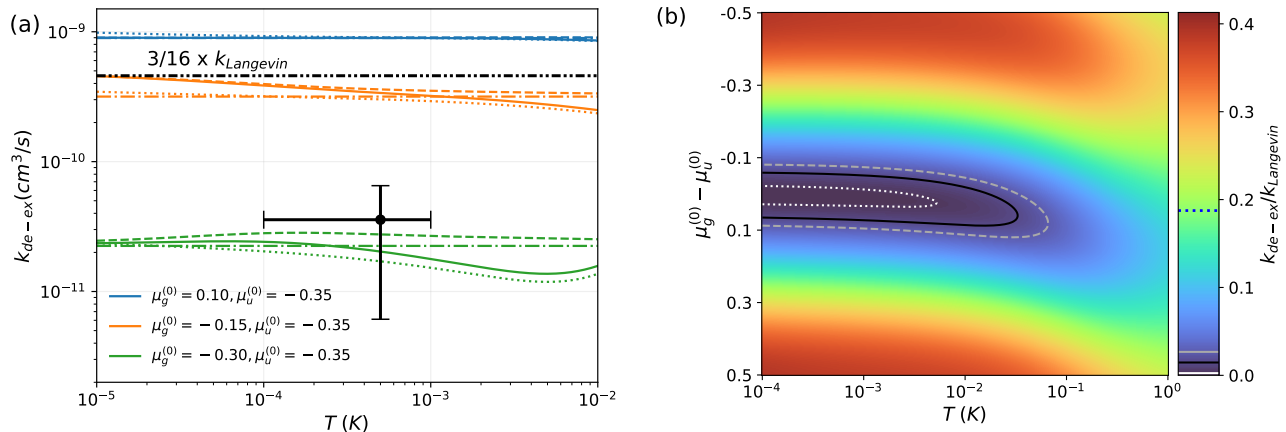


Figure 6. **Comparison of thermally averaged hyperfine de-excitation resonant charge-exchange (HDRCE) rate coefficients from calculations and experiment.** (a) The black point with uncertainty represents the experimentally measured rate coefficient. The solid lines correspond to calculations using full MQDT and l -dependent short-range parameters, while the dashed lines are calculated with full MQDT but without l -dependence in the short-range parameters. The dotted lines represent calculations using the semi-classical cross section in Eq. (20) with l -dependent short-range parameters. The dash-dotted lines correspond to the approximated semi-classical cross section in Eq. (21) without l -dependence in the short-range parameters. The three colors: blue, orange, and green, denote different sets of quantum defect parameters $\mu_{g,u}^{(0)}$ as indicated in the legend. The black dash-dotted line shows $3/16$ of the Langevin rate coefficient, corresponding to the classical limit of HDRCE for $^{87}\text{Rb} - ^{87}\text{Rb}^+$ (see Eq. (22)). (b) The color map shows rate coefficients calculated using the semi-classical cross section in Eq. (20). The energy and partial-wave dependence of the short range phases are extracted directly from Eq. (17). The solid black, dashed gray, and white dotted contours correspond to the center, upper bound, and lower bound of the measured rate coefficient, respectively. The blue dashed line on the colorbar indicates the classical value.

initio potentials (via the parameters β_g, β_u), but also with the approximate, semi-classical theoretical calculations using similar zero-energy s -wave quantum defects. Consequently, our measurements offer insights into the inter-atomic interactions in the ultracold s -wave regime, specifically the short-range scattering phase difference between the *gerade* and *ungerade* molecular states of the $^{87}\text{Rb} - ^{87}\text{Rb}^+$ complex.

The primary process leading to relaxation is the hyperfine interaction in combination with the charge-exchange process. The low collision rate strongly suppresses the probabilities of three-body processes. Additionally, electron spin relaxation is suppressed due to the large energy gap to higher energy levels. Finally, trap-induced dynamics [48, 73], which are accounted for in this analysis, can enhance cross sections at our collision temperature but cannot suppress them.

This result is remarkable given that our system, at temperatures of hundreds of $k_B \times \mu\text{K}$, is more than three orders of magnitude above the s -wave threshold energy, which is below $0.08 k_B \times \mu\text{K}$. The long range of the polarization potential interaction, which sets the s -wave limit to a low temperature, also makes the quantum nature of the reaction robust despite the involvement of many partial waves ($L \approx 12$).

While the exchange between $^{87}\text{Rb} - ^{87}\text{Rb}^+$ is suppressed in the cold regime, other isotopes or pairs of

alkali ions and their parent neutral atoms may exhibit different cross sections [22]. Owing to the sinusoidal dependence of the cross section on the relative phase shift (see, e.g., Eq. (21)), it is expected that most atom-ion pairs would deviate from the classical value (Eq. 22) if the differential phase shift is uniformly distributed, thus featuring either suppression or enhancement [22]. For instance, calculations of light elements have less theoretical uncertainty due to the smaller number of involved electrons. The hyperfine de-excitation rate coefficient in resonant charge-exchange collisions between singly ionized and neutral hydrogen atoms predict that $k_{\text{de-ex}} = k_L/3$ [82], indicating an enhancement over the classical limit ($k_{\text{de-ex}} \approx k_L/8$). Additionally, calculations of resonant charge-exchange collisions between lithium atoms and their parent ion show either suppression or enhancement of the resonant charge-exchange cross section depending on the isotope [96]. Furthermore, experiments studying quasi-resonant cold collisions of optically-accessible Yb isotopes estimated that charge-exchange collisions could saturate or exceed the Langevin rate [24]. However, we note that the observed cross section in these experiments could also be enhanced by trap-induced dynamics due to the formation of quasi bound states [48], which might require further investigation to estimate the properties of the short-range molecular potentials, similar to the analysis

carried out in this work (Sec. III C and Appendix A).

The application of the developed technique for calibrating the Langevin collision rate could allow accurate estimation of rates in other hybrid atom-ion systems. This work also provides the first demonstration of the quantum logic technique to study chemical reactions involving optically inaccessible atoms. It therefore opens the door to studying chemical complexes, whose properties cannot be computed with *ab initio* techniques.

For ion species with nonzero nuclear spins, enhanced coupling may allow for efficient preparation and detection of the nuclear spin state of a cold alkali ion, which is otherwise inaccessible owing to its isolation from the environment. Intriguingly, this isolation, which originates from the closed electronic shells and the small gyromagnetic ratio, is expected to grant long spin-coherence times, potentially enabling new applications in metrology or quantum information [97–100].

Note added: While this manuscript was under review, we applied the technique developed in this work to study spin-exchange collisions in an unpublished study [101] that focuses on small deviations from the phase-locking mechanism for collisions between neutral ^{87}Rb atoms and Sr^+ ions. It is emphasized that the present work represents our first experimental report reliably demonstrating the phase-locking mechanism.

ACKNOWLEDGMENTS

This work was supported by the Israeli Science Foundation and the Goldring Family Foundation. We thank Marko Cetina, Maks Walewski, Mathew Frye, and Michał Tomza for fruitful discussions.

Appendix A: Simulation of Collision Processes in the Trap

In this section, we detail the numerical simulations used to infer the Langevin collision rate from the data in Fig. 4, and the hyperfine de-excitation charge-exchange rate coefficient $k_{\text{de-ex}}$ from Fig. 4b. The ion positions as a function of time are modeled using the formalism described in Ref. [102], which accounts for secular motion and inherent micromotion due to trapping potentials, Coulomb forces between the ions, and dynamics associated with excess micromotion induced by static electric fields. The initial energy of the ion in the secular degrees of freedom is randomly sampled from the probability distribution function [103]

$$f(E) = \frac{E^2}{2k_B^3 T^3} \exp\left(-\frac{E}{k_B T}\right). \quad (\text{A1})$$

where T denotes the initial temperature.

We assume that during a single passage of the cloud, each ion in the chain may undergo Langevin collisions. The occurrence of these collisions follows Poissonian statistics with an average rate of κ_L , which is assumed to be independent of the collision energy. A Langevin-type collision is modeled as an instantaneous event occurring at a random time, where the ion's position remains unchanged, but its instantaneous velocity, \mathbf{v}_i , is updated to [47, 50]

$$\mathbf{v}_i \rightarrow (1 - r + \alpha r \mathcal{R}(\phi_L))(\mathbf{v}_i - \mathbf{v}_a) + \mathbf{v}_a, \quad (\text{A2})$$

where \mathbf{v}_a is the atom velocity, randomly drawn from a Maxwell-Boltzmann distribution with a temperature of $10 \mu\text{K}$, and $\alpha = 1$ for the neutral Rb atoms initialized in the lower hyperfine manifold ($F = 1$). The mass ratio is $r = \mu/m_i \approx 0.5$, where $\mu = m_i m_a / (m_i + m_a)$ is the reduced mass, and \mathcal{R} is the rotation matrix in the collision plane with a randomly generated scattering angle ϕ_L . The probability distribution function $f(\phi_L)$ for the scattering angle was calculated independently using classical scattering dynamics [77]. For spiraling collisions, we find that it is approximately given by $f(\phi_L) = 0.384 - 0.013\phi_L - 0.014\phi_L^2$ for $0 \leq \phi_L \leq \pi$.

The instantaneous change in velocity due to collisions redistributes the ion's micromotion energy into all directions, including the secular motion degrees of freedom. Denoting the amplitudes of the secular motion of the $^{88}\text{Sr}^+$ ion after the cloud passage as A_i , we calculate the detection probability of a bright $^{88}\text{Sr}^+$ ion as [47]

$$P_b = \cos^2\left(\frac{\pi}{2} \prod_i J_0(K_i A_i)\right), \quad (\text{A3})$$

assuming a detection pulse duration that is much longer than the motional cycle. Here, K_i denotes the components of the shelving beam's wavenumber along the

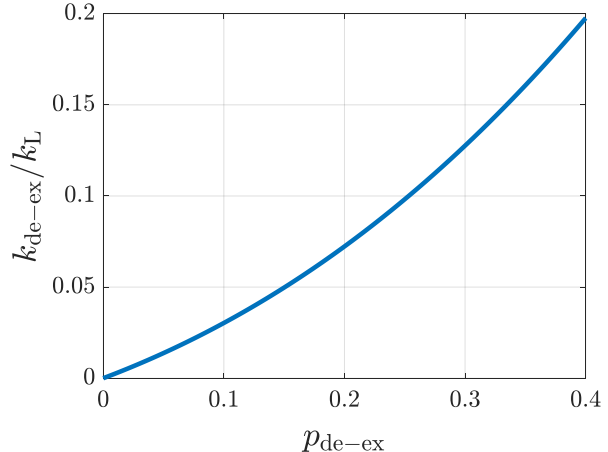


Figure 7. **Relationship between charge-exchange probability in the presence of the trap and in free space.** Numerical calculation of the measured hyperfine-changing charge-exchange probability per Langevin collision, $p_{\text{de-ex}}^{(^{87}\text{Rb}^+)}$, in the presence of the ion trap, as a function of the free-space ratio $k_{\text{de-ex}}/k_L$. The enhancement in the measured charge-exchange probability in the presence of the trap arises from trap-assisted bound states, which effectively increase the number of short range encounters associated with a single Langevin collision [48].

modes axes, and J_0 is the zeroth-order Bessel function. Notably, the sensitivity of our experimental and numerical techniques is limited to detecting secular motion along the shelving beam axis. We simulate the process approximately 5×10^4 times, averaging the results for each considered value of T and κ_L . The simulations show good agreement with the measured data in Fig. 4 for $T = 0.6 \pm 0.1 \text{ mK}$ and for $\kappa_L = 0.29 \pm 0.02$.

To estimate the effective microscopic hyperfine de-excitation probabilities, we repeat the simulations assuming full compensation of excess micromotion. This time, we assume the neutral ^{87}Rb atoms are in the upper hyperfine manifold ($F = 2$) and account for the hyperfine energy release by modifying the parameter α in Eq. A2. Specifically, with a probability $p_{\text{de-ex}}^{(\text{X})}$, α is updated to

$$\alpha = \sqrt{1 + 2r E_{\text{hpf}} / (m_i |\bar{v}_{\text{ion}}|^2)} \quad (\text{A4})$$

while retaining $\alpha = 1$ with a probability $1 - p_{\text{de-ex}}^{(\text{X})}$. Here, $\bar{v}_{\text{ion}} \equiv r(v_i - v_a)$ is the ion speed in the center-of-mass frame, and $\text{X} \in \{^{88}\text{Sr}^+, ^{87}\text{Rb}^+\}$ represents the ion species with which the neutral ^{87}Rb atom collides. Fitting this model to the data in Fig. 3, we find $p_{\text{de-ex}}^{(^{87}\text{Rb}^+)} = (0.053 \pm 0.04)$ per Langevin collision. This estimation approximately agrees with the rough approximation $p_{\text{de-ex}}^{(^{87}\text{Rb}^+)} \approx \bar{P}_{\text{hpf}}^{(\text{Rb})} / \kappa_L$.

To convert the probability $p_{\text{de-ex}}^{(87\text{Rb}^+)}$ into a rate coefficient (typically calculated for an atom and a free, untrapped ion), we account for trap dynamics during the collision process. The ion trap breaks translation invariance, enabling the formation of short-lived bound states during binary collisions of atom-ion pairs [48]. In these states, a single atom-ion pair can spiral and make close contact $n \geq 1$ times, potentially enhancing the measured inelastic or reaction rates compared to their free-space values. These effects are not captured by the earlier simulation, which assumes instantaneous collisions.

The likelihood of bound-state formation depends strongly on the initial collision energy of the atom-ion pair. For the experiments fitting κ_L via momentum-changing collisions, the initial energy is sufficiently high such that quasi-bound states have negligible effect. However, in hyperfine de-excitation experiments, the initial energy is low enough that these bound states play a significant role. Bound state formation enhances the measured rate but does not reverse a reaction, since

the energy released during a hyperfine de-excitation collision effectively breaks the weakly bound molecule.

Due to the release of hyperfine energy, the free-space probability $k_{\text{de-ex}}/k_L$ for hyperfine de-excitation collisions relates to the effective measured probability in the presence of the trap as:

$$p_{\text{de-ex}} = \sum_n \text{PMF}(n) \sum_{m=1}^n \left(1 - \frac{k_{\text{de-ex}}}{k_L}\right)^{m-1} \left(\frac{k_{\text{de-ex}}}{k_L}\right). \quad (\text{A5})$$

where $\text{PMF}(n)$ is the probability mass function of n , the number of close encounters during the quasi-bound state lifetime. We simulate the effect of bound states in our trap using the molecular dynamics approach described in Ref. [48], reconstructing $\text{PMF}(n)$ from approximately 2500 Langevin collisions. From this probability distribution, we derive the relationship between the microscopic exchange probability under trap conditions and the rate coefficient in free space, as shown in Fig. 7. This analysis establishes the relationship between $k_{\text{de-ex}}$ and k_L , as discussed in the main text.

-
- [1] P. Paliwal, N. Deb, D. M. Reich, A. v. d. Avoird, C. P. Koch, and E. Narevicius, Determining the nature of quantum resonances by probing elastic and reactive scattering in cold collisions, *Nature Chemistry* **13**, 94 (2021).
- [2] T. Köhler, K. Góral, and P. S. Julienne, Production of cold molecules via magnetically tunable feshbach resonances, *Reviews of modern physics* **78**, 1311 (2006).
- [3] C. Chin, R. Grimm, P. Julienne, and E. Tiesinga, Feshbach resonances in ultracold gases, *Reviews of Modern Physics* **82**, 1225 (2010).
- [4] I. Bloch, J. Dalibard, and S. Nascimbene, Quantum simulations with ultracold quantum gases, *Nature Physics* **8**, 267 (2012).
- [5] F. Schäfer, T. Fukuhara, S. Sugawa, Y. Takasu, and Y. Takahashi, Tools for quantum simulation with ultracold atoms in optical lattices, *Nature Reviews Physics* **2**, 411 (2020).
- [6] K. Jachymski and A. Negretti, Quantum simulation of extended polaron models using compound atom-ion systems, *Physical Review Research* **2**, 033326 (2020).
- [7] C. Gross, T. Zibold, E. Nicklas, J. Esteve, and M. K. Oberthaler, Nonlinear atom interferometer surpasses classical precision limit, *Nature* **464**, 1165 (2010).
- [8] M. Safronova, D. Budker, D. DeMille, D. F. J. Kimball, A. Derevianko, and C. W. Clark, Search for new physics with atoms and molecules, *Reviews of Modern Physics* **90**, 025008 (2018).
- [9] S. Kondov, C.-H. Lee, M. McDonald, B. McGuyer, I. Majewska, R. Moszynski, and T. Zelevinsky, Crossover from the ultracold to the quasiclassical regime in state-selected photodissociation, *Physical Review Letters* **121**, 143401 (2018).
- [10] I. Majewska, S. Kondov, C.-H. Lee, M. McDonald, B. McGuyer, R. Moszynski, and T. Zelevinsky, Experimental and theoretical investigation of the crossover from the ultracold to the quasiclassical regime of photodissociation, *Physical Review A* **98**, 043404 (2018).
- [11] K. M. Jones, E. Tiesinga, P. D. Lett, and P. S. Julienne, Ultracold photoassociation spectroscopy: Long-range molecules and atomic scattering, *Reviews of Modern Physics* **78**, 483 (2006).
- [12] S. Ospelkaus, K.-K. Ni, D. Wang, M. De Miranda, B. Neyenhuis, G. Quémener, P. Julienne, J. Bohn, D. Jin, and J. Ye, Quantum-state controlled chemical reactions of ultracold potassium-rubidium molecules, *Science* **327**, 853 (2010).
- [13] Y. Liu, M.-G. Hu, M. A. Nichols, D. Yang, D. Xie, H. Guo, and K.-K. Ni, Precision test of statistical dynamics with state-to-state ultracold chemistry, *Nature* **593**, 379 (2021).
- [14] F. Schmidt, D. Mayer, Q. Bouton, D. Adam, T. Lausch, J. Nettersheim, E. Tiemann, and A. Widera, Tailored single-atom collisions at ultralow energies, *Physical Review Letters* **122**, 013401 (2019).
- [15] P. Weckesser, F. Thielemann, D. Wiater, A. Wojciechowska, L. Karpa, K. Jachymski, M. Tomza, T. Walker, and T. Schaetz, Observation of feshbach resonances between a single ion and ultracold atoms, *Nature* **600**, 429 (2021).
- [16] T. Feldker, H. FÜRst, H. Hirzler, N. Ewald, M. Mazzanti, D. Wiater, M. Tomza, and R. Gerritsma, Buffer gas cooling of a trapped ion to the quantum regime, *Nature Physics* **16**, 413 (2020).
- [17] K. Jachymski, M. Krych, P. S. Julienne, and Z. Idziaszek, Quantum-defect model of a reactive collision at finite temperature, *Physical Review A* **90**, 042705 (2014).

- [18] M. Tomza, K. Jachymski, R. Gerritsma, A. Negretti, T. Calarco, Z. Idziaszek, and P. S. Julienne, Cold hybrid ion-atom systems, *Reviews of modern physics* **91**, 035001 (2019).
- [19] M. Cetina, A. T. Grier, and V. Vuletić, Micromotion-induced limit to atom-ion sympathetic cooling in paul traps, *Physical review letters* **109**, 253201 (2012).
- [20] M. Pinkas, Z. Meir, T. Sikorsky, R. Ben-Shlomi, N. Akerman, and R. Ozeri, Effect of ion-trap parameters on energy distributions of ultra-cold atom-ion mixtures, *New Journal of Physics* **22**, 013047 (2020).
- [21] R. S. Lous and R. Gerritsma, Ultracold ion-atom experiments: cooling, chemistry, and quantum effects, *Advances in Atomic, Molecular, and Optical Physics* **71**, 65 (2022).
- [22] R. Côté and I. Simbotin, Signature of the s-wave regime high above ultralow temperatures, *Physical Review Letters* **121**, 173401 (2018).
- [23] T. Sikorsky, M. Morita, Z. Meir, A. A. Buchachenko, R. Ben-Shlomi, N. Akerman, E. Narevicius, T. V. Tscherbul, and R. Ozeri, Phase locking between different partial waves in atom-ion spin-exchange collisions, *Physical review letters* **121**, 173402 (2018).
- [24] A. T. Grier, M. Cetina, F. Oručević, and V. Vuletić, Observation of cold collisions between trapped ions and trapped atoms, *Physical review letters* **102**, 223201 (2009).
- [25] J. Schmidt, P. Weckesser, F. Thielemann, T. Schaetz, and L. Karpa, Optical traps for sympathetic cooling of ions with ultracold neutral atoms, *Physical review letters* **124**, 053402 (2020).
- [26] L. Ratschbacher, C. Zipkes, C. Sias, and M. Köhl, Controlling chemical reactions of a single particle, *Nature Physics* **8**, 649 (2012).
- [27] A. Härter and J. Hecker Denschlag, Cold atom-ion experiments in hybrid traps, *Contemporary Physics* **55**, 33 (2014).
- [28] F. H. Hall, M. Aymar, N. Bouloufa-Maafa, O. Dulieu, and S. Willitsch, Light-assisted ion-neutral reactive processes in the cold regime: Radiative molecule formation versus charge exchange, *Physical review letters* **107**, 243202 (2011).
- [29] T. Sikorsky, Z. Meir, R. Ben-Shlomi, N. Akerman, and R. Ozeri, Spin-controlled atom-ion chemistry, *Nature communications* **9**, 1 (2018).
- [30] A. Mohammadi, A. Krüchow, A. Mahdian, M. Deiß, J. Pérez-Ríos, H. da Silva Jr, M. Raoult, O. Dulieu, and J. H. Denschlag, Life and death of a cold barb^+ molecule inside an ultracold cloud of rb atoms, *Physical Review Research* **3**, 013196 (2021).
- [31] W. G. Rellergert, S. T. Sullivan, S. Kotochigova, A. Petrov, K. Chen, S. J. Schowalter, and E. R. Hudson, Measurement of a large chemical reaction rate between ultracold closed-shell ca 40 atoms and open-shell $\text{yb}^+ 174$ ions held in a hybrid atom-ion trap, *Physical review letters* **107**, 243201 (2011).
- [32] T. V. Tscherbul, P. Brumer, and A. A. Buchachenko, Spin-orbit interactions and quantum spin dynamics in cold ion-atom collisions, *Physical Review Letters* **117**, 143201 (2016).
- [33] R. Saito, S. Haze, M. Sasakawa, R. Nakai, M. Raoult, H. Da Silva Jr, O. Dulieu, and T. Mukaiyama, Characterization of charge-exchange collisions between ultracold li 6 atoms and ca 40+ ions, *Physical Review A* **95**, 032709 (2017).
- [34] A. Krüchow, A. Mohammadi, A. Härter, J. H. Denschlag, J. Pérez-Ríos, and C. H. Greene, Energy scaling of cold atom-atom-ion three-body recombination, *Physical Review Letters* **116**, 193201 (2016).
- [35] H. Hirzler, R. Lous, E. Trimby, J. Pérez-Ríos, A. Safavi-Naini, and R. Gerritsma, Observation of chemical reactions between a trapped ion and ultracold feshbach dimers, *Physical Review Letters* **128**, 103401 (2022).
- [36] F. H. Hall and S. Willitsch, Millikelvin reactive collisions between sympathetically cooled molecular ions and laser-cooled atoms in an ion-atom hybrid trap, *Physical review letters* **109**, 233202 (2012).
- [37] M. Tomza and M. Lisaj, Interactions and charge-transfer dynamics of an al^+ ion immersed in ultracold rb and sr atoms, *Physical Review A* **101**, 012705 (2020).
- [38] H. Li, S. Jyothi, M. Li, J. Kłos, A. Petrov, K. R. Brown, and S. Kotochigova, Photon-mediated charge exchange reactions between 39 k atoms and 40 ca+ ions in a hybrid trap, *Physical Chemistry Chemical Physics* **22**, 10870 (2020).
- [39] N. Ewald, T. Feldker, H. Hirzler, H. Fürst, and R. Gerritsma, Observation of interactions between trapped ions and ultracold rydberg atoms, *Physical Review Letters* **122**, 253401 (2019).
- [40] S. Haze, R. Saito, M. Fujinaga, and T. Mukaiyama, Charge-exchange collisions between ultracold fermionic lithium atoms and calcium ions, *Physical Review A* **91**, 032709 (2015).
- [41] S. Schmid, A. Härter, and J. H. Denschlag, Dynamics of a cold trapped ion in a bose-einstein condensate, *Physical review letters* **105**, 133202 (2010).
- [42] P. F. Staunum, K. Højbjerg, R. Wester, and M. Drewsen, Probing isotope effects in chemical reactions using single ions, *Physical review letters* **100**, 243003 (2008).
- [43] I. Sivarajah, D. Goodman, J. Wells, F. Narducci, and W. Smith, Evidence of sympathetic cooling of na^+ ions by a na magneto-optical trap in a hybrid trap, *Physical Review A* **86**, 063419 (2012).
- [44] K. S. Kleinbach, F. Engel, T. Dieterle, R. Löw, T. Pfau, and F. Meinert, Ionic impurity in a bose-einstein condensate at submicrokelvin temperatures, *Physical review letters* **120**, 193401 (2018).
- [45] R. Ben-shlomi, R. Vexiau, Z. Meir, T. Sikorsky, N. Akerman, M. Pinkas, O. Dulieu, and R. Ozeri, Direct observation of ultracold atom-ion excitation exchange, *Physical Review A* **102**, 031301(R) (2020).
- [46] R. Ben-shlomi, M. Pinkas, Z. Meir, T. Sikorsky, O. Katz, N. Akerman, and R. Ozeri, High-energy-resolution measurements of an ultracold-atom-ion collisional cross section, *Physical Review A* **103**, 032805 (2021).
- [47] O. Katz, M. Pinkas, N. Akerman, and R. Ozeri, Quantum logic detection of collisions between single atom-ion pairs, *Nature Physics* **18**, 533 (2022).
- [48] M. Pinkas, O. Katz, J. Wengrowicz, N. Akerman, and R. Ozeri, Trap-assisted formation of atom-ion bound

- states, *Nature Physics* **19**, 1573 (2023).
- [49] P. Langevin, Une formule fondamentale de theorie cinetique, *Ann. Chim. Phys.* **5** (1905).
- [50] C. Zipkes, L. Ratschbacher, C. Sias, and M. Köhl, Kinetics of a single trapped ion in an ultracold buffer gas, *New Journal of Physics* **13**, 053020 (2011).
- [51] A. Dalgarno and M. Rudge, Spin-change cross-sections for collisions between alkali atoms, *Proceedings of the Royal Society of London. Series A. Mathematical and Physical Sciences* **286**, 519 (1965).
- [52] A. Dalgarno, M. C. McDowell, and A. Williams, The mobilities of ions in unlike gases, *Philosophical Transactions of the Royal Society of London. Series A, Mathematical and Physical Sciences* **250**, 411 (1958).
- [53] A. Dalgarno and D. R. Bates, The mobilities of ions in their parent gases, *Philosophical Transactions of the Royal Society of London. Series A, Mathematical and Physical Sciences* **250**, 426 (1958).
- [54] N. F. Mott and H. S. W. Massey, *Theory of atomic collisions, Theory of Atomic Collisions* (1933).
- [55] H. Massey and R. Smith, The passage of positive ions through gases, *Proceedings of the Royal Society of London. Series A, Containing Papers of a Mathematical and Physical Character* **142**, 142 (1933).
- [56] J. Hasted, The exchange of charge between ions and atoms, *Proceedings of the Royal Society of London. Series A. Mathematical and Physical Sciences* **205**, 421 (1951).
- [57] D. Rapp and W. E. Francis, Charge exchange between gaseous ions and atoms, *The Journal of Chemical Physics* **37**, 2631 (1962).
- [58] W. Lichten, Resonant charge exchange in atomic collisions, *Physical Review* **131**, 229 (1963).
- [59] W. Lichten, Resonant charge exchange in atomic collisions. ii. further applications and extension to the quasi-resonant case, *Physical Review* **139**, A27 (1965).
- [60] R. Côté and A. Dalgarno, Ultracold atom-ion collisions, *Physical Review A* **62**, 012709 (2000).
- [61] A. Dalgarno, Spin-change cross-sections, *Proceedings of the Royal Society of London. Series A. Mathematical and Physical Sciences* **262**, 132 (1961).
- [62] R. Côté, Ultracold hybrid atom–ion systems, in *Advances in atomic, molecular, and optical physics*, Vol. 65 (Elsevier, 2016) pp. 67–126.
- [63] K. Ravi, S. Lee, A. Sharma, G. Werth, and S. Rangwala, Cooling and stabilization by collisions in a mixed ion–atom system, *Nature Communications* **3**, 1 (2012).
- [64] S. Dutta and S. Rangwala, Cooling of trapped ions by resonant charge exchange, *Physical Review A* **97**, 041401 (2018).
- [65] A. Mahdian, A. Krüchow, and J. H. Denschlag, Direct observation of swap cooling in atom–ion collisions, *New Journal of Physics* **23**, 065008 (2021).
- [66] J. K. Mitchell and E. N. Fortson, Optical-pumping charge-exchange method for studying nuclear-spin orientation in s 0 1 atomic ions, *Physical Review A* **8**, 704 (1973).
- [67] S. S. Townsend, *Charge Exchange Optical Pumping.*, Ph.D. thesis, University of New Hampshire (1977).
- [68] A. Härter, A. Krüchow, A. Brunner, W. Schnitzler, S. Schmid, and J. H. Denschlag, Single ion as a three-body reaction center in an ultracold atomic gas, *Physical review letters* **109**, 123201 (2012).
- [69] Charge exchange at high collision energies is often characterized by backward scattering, with a peak in the scattering cross section at scattering angles $\theta \approx \pi$, while elastic contributions are often attributed to forward scattering, at angles $\theta \approx 0$. See, e.g., ch. 3 in Ref. [62] or Ref. [104] for details. In the cold regime, however, the spiraling nature of Langevin collisions renders the scattering angles θ more uniform, making it difficult to distinguish elastic from charge-exchange contributions based on the momentum changes.
- [70] J. R. Zimmerman and D. Williams, Determination of nuclear gyromagnetic ratios i , *Physical Review* **76**, 350 (1949).
- [71] W. Paul, Electromagnetic traps for charged and neutral particles, *Reviews of Modern Physics* **62**, 531 (1990).
- [72] Z. Meir, T. Sikorsky, R. Ben-shlomi, N. Akerman, M. Pinkas, Y. Dallal, and R. Ozeri, Experimental apparatus for overlapping a ground-state cooled ion with ultracold atoms, *Journal of Modern Optics* **65**, 501 (2018).
- [73] H. Hirzler, E. Trimby, R. Gerritsma, A. Safavi-Naini, and J. Pérez-Ríos, Trap-assisted complexes in cold atom-ion collisions, *Physical Review Letters* **130**, 143003 (2023).
- [74] K. Chen, S. T. Sullivan, and E. R. Hudson, Neutral gas sympathetic cooling of an ion in a paul trap, *Physical review letters* **112**, 143009 (2014).
- [75] Z. Meir, M. Pinkas, T. Sikorsky, R. Ben-shlomi, , N. Akerman, , and R. Ozeri, Direct observation of atom-ion nonequilibrium sympathetic cooling, *Physical Review Letters* **121**, 053402 (2018).
- [76] We adopt the definitions in Ref. [74] which distinguishes momentum-changing collisions from elastic glancing collisions. The latter are predominantly forward-scattering events and barely redistribute the kinetic energy (c.f. [75, 105]).
- [77] M. Cetina *et al.*, *Hybrid approaches to quantum information using ions, atoms and photons*, Ph.D. thesis, Massachusetts Institute of Technology (2011).
- [78] D. Leibfried, R. Blatt, C. Monroe, and D. Wineland, Quantum dynamics of single trapped ions, *Reviews of Modern Physics* **75**, 281 (2003).
- [79] A. Jrajai, A.-R. Allouche, M. Korek, and M. Aubert-Frécon, Theoretical electronic structure of the alkali-dimer cation rb_2^+ , *Chemical physics* **290**, 129 (2003).
- [80] J. Schnabel, L. Cheng, and A. Köhn, High-accuracy rb_2^+ interaction potentials based on coupled-cluster calculations, *Phys. Rev. A* **106**, 032804 (2022).
- [81] M. Li, L. You, and B. Gao, Multichannel quantum-defect theory for ion-atom interactions, *Phys. Rev. A* **89**, 052704 (2014).
- [82] M. Li and B. Gao, Proton-hydrogen collisions at low temperatures, *Phys. Rev. A* **91**, 032702 (2015).
- [83] B. Gao, Theory of slow-atom collisions, *Phys. Rev. A* **54**, 2022 (1996).
- [84] P. Schwerdtfeger and J. K. Nagle, 2018 table of static dipole polarizabilities of the neutral elements in the periodic table, *Molecular Physics* **117**, 1200 (2019).
- [85] M. D. Gregoire, N. Brooks, R. Trubko, and A. D. Cronin, Analysis of polarizability measure-

- ments made with atom interferometry, *Atoms* **4**, 10.3390/atoms4030021 (2016).
- [86] B. Gao, General form of the quantum-defect theory for- $1/r$ α type of potentials with $\alpha > 2$, *Phys. Rev. A* **78**, 012702 (2008).
- [87] C. Greene, U. Fano, and G. Strinati, General form of the quantum-defect theory, *Phys. Rev. A* **19**, 1485 (1979).
- [88] C. H. Greene, A. R. P. Rau, and U. Fano, General form of the quantum-defect theory. ii, *Phys. Rev. A* **26**, 2441 (1982).
- [89] M. J. Seaton, Quantum defect theory, *Reports on Progress in Physics* **46**, 167 (1983).
- [90] U. Fano and A. Rau, *Atomic Collisions and Spectra* (Academic Press, 1986).
- [91] M. Aymar, C. H. Greene, and E. Luc-Koenig, Multi-channel rydberg spectroscopy of complex atoms, *Rev. Mod. Phys.* **68**, 1015 (1996).
- [92] B. Gao, E. Tiesinga, C. J. Williams, and P. S. Julienne, Multichannel quantum-defect theory for slow atomic collisions, *Phys. Rev. A* **72**, 042719 (2005).
- [93] B. Gao, Quantum-defect theory for- $1/r$ 4-type interactions, *Phys. Rev. A* **88**, 022701 (2013).
- [94] M. Beyer and F. Merkt, Hyperfine-interaction-induced g/u mixing and its implication on the existence of the first excited vibrational level of the $a^+ \sigma u + 2$ state of h_2^+ and on the scattering length of the $h + h^+$ collision, *The Journal of Chemical Physics* **149** (2018).
- [95] A. Green, J. H. See Toh, R. Roy, M. Li, S. Kotochigova, and S. Gupta, Two-photon photoassociation spectroscopy of the $^2\Sigma^+$ $ybli$ molecular ground state, *Phys. Rev. A* **99**, 063416 (2019).
- [96] N. Joshi, M. Niranjana, A. Pandey, O. Dulieu, R. Côté, and S. Rangwala, Homonuclear ion-atom collisions: Application to $li^+ - li$, *Physical Review A* **105**, 063311 (2022).
- [97] P. Wang, C.-Y. Luan, M. Qiao, M. Um, J. Zhang, Y. Wang, X. Yuan, M. Gu, J. Zhang, and K. Kim, Single ion qubit with estimated coherence time exceeding one hour, *Nature communications* **12**, 1 (2021).
- [98] R. Shaham, O. Katz, and O. Firstenberg, Strong coupling of alkali-metal spins to noble-gas spins with an hour-long coherence time, *Nature Physics* **18**, 506 (2022).
- [99] O. Katz, R. Shaham, and O. Firstenberg, Coupling light to a nuclear spin gas with a two-photon linewidth of five millihertz, *Science advances* **7**, eabe9164 (2021).
- [100] O. Katz, R. Shaham, E. Reches, A. V. Gorshkov, and O. Firstenberg, Optical quantum memory for noble-gas spins based on spin-exchange collisions, *Physical Review A* **105**, 042606 (2022).
- [101] M. Z. Walewski, M. D. Frye, O. Katz, M. Pinkas, R. Ozeri, and M. Tomza, Quantum control of ion-atom collisions beyond the ultracold regime, *arXiv preprint arXiv:2407.06073* (2024).
- [102] A. Bermudez, P. Schindler, T. Monz, R. Blatt, and M. Müller, Micromotion-enabled improvement of quantum logic gates with trapped ions, *New Journal of Physics* **19**, 113038 (2017).
- [103] Z. Meir, *Dynamics of a single, ground-state cooled and trapped ion colliding with ultracold atoms: a micromotion tale*, Ph.D. thesis, The Weizmann Institute of Science (Israel) (2017).
- [104] B. Bransden, The theory of charge exchange, *Reports on Progress in Physics* **35**, 949 (1972).
- [105] C. Zipkes, S. Palzer, L. Ratschbacher, C. Sias, and M. Köhl, Cold heteronuclear atom-ion collisions, *Physical review letters* **105**, 133201 (2010).